



HAL
open science

Numerical Reconstruction of Landslide Paleotsunami using Geological Records in Alpine Lake Aiguebelette

Muhammad Naveed Zafar, Denys Dutykh, Pierre Sabatier, Mathilde Banjan,
Jihwan Kim

► **To cite this version:**

Muhammad Naveed Zafar, Denys Dutykh, Pierre Sabatier, Mathilde Banjan, Jihwan Kim. Numerical Reconstruction of Landslide Paleotsunami using Geological Records in Alpine Lake Aiguebelette. *Journal of Geophysical Research: Solid Earth*, 2024, Volume 129 (e2023JB028629), 10.1029/2023JB028629 . hal-04592536

HAL Id: hal-04592536

<https://hal.science/hal-04592536v1>

Submitted on 29 May 2024

HAL is a multi-disciplinary open access archive for the deposit and dissemination of scientific research documents, whether they are published or not. The documents may come from teaching and research institutions in France or abroad, or from public or private research centers.

L'archive ouverte pluridisciplinaire **HAL**, est destinée au dépôt et à la diffusion de documents scientifiques de niveau recherche, publiés ou non, émanant des établissements d'enseignement et de recherche français ou étrangers, des laboratoires publics ou privés.



Distributed under a Creative Commons Attribution - NonCommercial - NoDerivatives 4.0
International License



AGU Word Manuscript Template

Numerical Reconstruction of Landslide Paleotsunami using Geological Records in Alpine Lake Aiguebelette

Muhammad Naveed Zafar^{1,2}, Denys Dutykh^{3,4}, Pierre Sabatier², Mathilde Banjan^{2,5}, and Jihwan Kim⁶

¹LAMA, Univ. Grenoble Alpes, Univ. Savoie Mont Blanc, CNRS, Chambéry, France

²EDYTEM, Univ. Savoie Mont Blanc, CNRS, 73370 Le Bourget-du-Lac, France

³Mathematics Department, Khalifa University of Science and Technology, PO Box 127788, Abu Dhabi, United Arab Emirates

⁴Causal Dynamics Pty Ltd, Perth, Australia

⁵ISTerre, Univ. Savoie Mont Blanc, Univ. Grenoble Alpes, CNRS, IRD, Univ. Gustave Eiffel, Le Bourget du lac, France

⁶Instituto Portugues do Mar e da Atmosfera (IPMA), Lisbon, Portugal

Key Points:

- Uncovered a 11,700-year-old subaqueous landslide-induced paleotsunami in Lake Aiguebelette (NW Alps, France)
- Numerical model is constrained to reproduce the available geological data
- Found dispersion effects to be of minimal importance in the modeling of this historical tsunami event

Abstract

Mass movements and delta collapses are significant sources of tsunamis in lacustrine environments, impacting human societies enormously. Paleotsunamis studies play an essential role in understanding historical events and their consequences, along with their return periods. This study investigates a paleotsunami induced by a subaqueous mass movement during the Younger Dryas to Early Holocene transition, *ca.* 11,700 years ago in Lake Aiguebelette (NW Alps, France). Utilizing high-resolution seismic and bathymetric surveys associated with sedimentological, geochemical, and magnetic analyses, we uncovered a paleotsunami triggered by a seismically induced mass transport deposit. Numerical simulations of mass movement have been conducted using a visco-plastic Herschel-Bulkley rheological model and corresponding tsunami wave modeled with dispersive and nondispersive models. Our findings reveal for the first time that dispersive effects may be negligible for subaqueous landslides in a relatively small lake. This research reconstructs a previously unreported paleotsunami event and enhances our understanding of tsunami dynamics in lacustrine environments.

Plain Language Summary

This study explores an ancient landslide and its ability to potentially generate a tsunami. This event took place in Lake Aiguebelette, located in the NW Alps, France. By applying advanced underwater mapping techniques and computer modeling, we were able to reconstruct the origins and impact of this underwater prehistoric landslide. Our work revealed that this underwater landslide may have triggered a significant tsunami wave. These findings are crucial as they provide new insights into the dynamics of such geological events in lake environments, enhancing our understanding of their potential impacts and aiding in the preparation for future similar hazards.

1 Introduction

The most common geophysical disturbances that trigger tsunamis are earthquakes, landslides, or their combinations. Tsunamis can vary widely in size, and their extent depends on the characteristics of these geophysical perturbations. Earthquake tsunamis are the most significant and global tsunamis, with large wavelengths up to thousands of kilometers and relatively small amplitudes (Kanamori, 1972; Abe, 1973; Ward, 1980; Okal, 1988; Dutykh et al., 2006; Kervella et al., 2007; Dutykh & Dias, 2007; Dias et al., 2014). On the other hand, tsunamis caused by mass movement related to landslides (Hampton et al., 1996; Ward, 2001) or volcanic collapses (Kienle et al., 1987; Pararas-Carayannis, 1992; Paris, 2015) are generally more localized. However, they have the potential to generate large tsunami waves (Bardet et al., 2003; Beizel et al., 2012; Dutykh & Kalisch, 2013; Løvholt et al., 2015; Waldmann et al., 2021). They are complicated and more diverse, although their wavelength can measure several hundred of meters, much shorter than earthquake tsunamis (Harbitz et al., 2006; Dutykh et al., 2013). Therefore, compared to earthquake tsunamis, prognostic analysis is less developed for mass-movement tsunamis. Thus, we have a limited understanding of this type of tsunami hazard. One reason for this lack of knowledge is that tsunamis triggered by landslides are much less reported in catalogs than earthquakes (Behrens et al., 2021; Roger et al., 2024), so there are limited records available (Blikra et al., 2005; Yamada et al., 2012; Kremer et al., 2015, 2012, 2021; Lane et al., 2017; Urgeles & Camerlenghi, 2013; Waldmann et al., 2021; Nigg et al., 2021).

Subaerial or subaqueous mass transport deposits can generate destructive tsunamis. Among the most devastating subaerial landslide-induced tsunamis are the 1958 Lituya Bay tsunami, which produced the highest runup height of 524 meters (Miller, 1960), and the 1963 Vajont Dam tsunami in Italy, which generated a massive wave with runup height of 270 meters and killed around 2000 people (Bosa & Petti, 2011). These events highlight the importance of studying landslide-induced tsunamis to predict better and reduce tsunami risks. Tsunamis triggered by subaqueous mass movement are also receiving significant attention as natural hazards that pose a risk to coastal communities (Bardet et al., 2003; Satake, 2012). Substantial regional coseismic displacements or volcanic eruptions can trigger subaqueous mass movements. Depending on the size and characteristics of the mass movement and the bathymetric setting, these mass failures may be tsunamigenic (Urgeles & Camerlenghi, 2013; Dutykh & Kalisch, 2013; Løvholt et al., 2015, 2017; Kim et al., 2019). One recent example of such a tsunami is the 1998 Papua New Guinea tsunami (Tappin et al., 2001; Synolakis et al., 2002; Lynett et al., 2003), generated by seismically triggered subaqueous mass movements. This catastrophic event, characterized by a maximal local runup of 15 meters, resulted in the tragic loss of over 2,000 lives. Other examples include the event of 1994 at Skagway, Alaska (Kulikov et al., 1996; Rabinovich et al., 1999; Thomson et al., 2001) and 1979 at Nice Airport, France (Assier-Rzadkiewicz et al., 2000; Dan et al., 2007). Studying paleotsunamis are crucial to understanding their patterns over time. Geological archives including onshore and offshore sedimentary deposits serve as primary and reliable sources of evidence. Researchers can use these geological archives to reconstruct past events and estimate the frequency and magnitude of historical

events (Nanayama et al., 2003; Paris et al., 2007; Goto et al., 2011; Sugawara et al., 2014; Chagué-Goff et al., 2017; Biguenet et al., 2021; Cordrie et al., 2022).

The study of marine paleotsunami sediments has been the focus of attention in recent decades, with numerous publications documenting the investigation of paleotsunami sediment archives at several marine sites. They investigated the recurrence rate (Monecke et al., 2008; Migeon et al., 2017; Kempf et al., 2017) and runup height (Bondevik et al., 1997; Petersone et al., 2011) and determined the inundation distance of past tsunami events using sedimentary records (Switzer et al., 2012; Abe et al., 2012; Goto et al., 2019; Ishimura & Yamada, 2019; Paris et al., 2023). However, investigating their lacustrine counterparts has received little attention so far (Sammartini et al., 2019; Kremer et al., 2021; 2012, Nigg et al., 2021). Mechanisms of tsunami generation by mass movements are not limited to the marine environment; they also occur in different lacustrine settings, *e.g.*, fjord-type lakes or fault-bounded basin lakes, which have large mass movements relative to the lake basin. Several historical sublacustrine mass movement induced-tsunami events have been documented, such as Lake Tahoe in USA (Moore et al., 2014), Lake Tekapo in New Zealand (Mountjoy et al., 2019), Lake Nahuel Huapi in Argentina (Beigt et al., 2016) and various Alpine lakes in Switzerland, including Lake Geneva (Kremer et al., 2012), Lake Lauers (Bussmann & Anselmetti, 2010), Lake Lucerne (Hilbe & Anselmetti, 2014), Lake Brienz (Girardclos et al., 2007) and Lake Sils (Nigg et al., 2021). Sediment archives are the only way to gain deeper insight into these events, and geoscientists can reconstruct these low-frequency events using sediment records. Several mass-movement events have been reconstructed in pre-Alpine lakes based on geophysical and sedimentological evidence that transport large amounts of sediments from lateral slopes to deep basins (Van Rensbergen et al., 1998; Chapron et al., 1999; Strasser & F. Anselmetti, 2008; Beck, 2009; Wilhelm et al., 2013). Some of these events occurred in the Younger Dryas–Early Holocene (YD-EH) transition time range, such as Lake Bourget (close to Lake Aiguebelette) and Lake Annecy, and were studied using seismic reflection surveys. Here, we focus on one of these types of mass-movement events discovered in Lake Aiguebelette (NW French Alps) at the YD-EH climate transition (Banjan et al., 2022). This event was identified thanks to high-resolution seismic and bathymetric data associated with sedimentary, geochemical, and magnetic proxies on sediment cores. Such events were interpreted as seismically-induced. Seismic activity is enhanced by rapid climate change and glacial retreat, such as crustal rebound and erosional unloading at this climate transition (Banjan et al., 2022).

Numerical modeling of tsunamis serves as an alternative method for estimating potential tsunami hazards when direct measurements are absent. Numerical modeling of paleotsunamis is an indispensable part of multidisciplinary research that bridges the gap between practical applications of tsunami sediments and geological studies (Jaffe et al., 2016). This research aims to conduct the first numerical study of French-Alpine lake Aiguebelette to reconstruct paleo-mass-movement events and investigate whether this reconstructed mass movement could generate tsunamis. Additionally, we discuss the characteristics and dynamics of past tsunamis and how they interact with relatively small lacustrine environments. This research study is also relevant for other pre-Alpine lakes that exhibit similar sublacustrine mass movements (Rapuc et al., 2022; Fanetti et al., 2008) and associated tsunami hazards.

The present manuscript is organized as follows. A description of the study site and sedimentary sequence is provided in Section 2. Then (Section 3), we use the Herschel-Bulkley rheological landslide model, which is coupled with dispersive and nondispersive tsunami wave models. Simulation results for mass transport deposits, tsunami propagation, and inundation along Froude number estimation are presented in Section 4. We discuss our results, particularly the validation of the simulations with geological observations and the dispersion effect for sublacustrine landslides in Section 5. The paper concludes in the final Section 6, summarizing our current research and outlining future perspectives.

2 Study Site and Lake Sedimentary Sequences

Lake Aiguebelette is a pre-Alpine lake that formed after glaciers retreat. It is located in the northwestern Alps (France), at an elevation of 373 m above sea level with a surface area of 5.45 km². The lake's average depth is 30 m, and the maximum depth of the deepest basin is approximately 70 m. The 'Leysse de Novalaise' is the main tributary entering the lake's northern part. The geology of the catchment area is presented in Fig. 1a (further detailed in Banjan et al. (2022)), while Fig. 1b shows an aerial view of the lake.

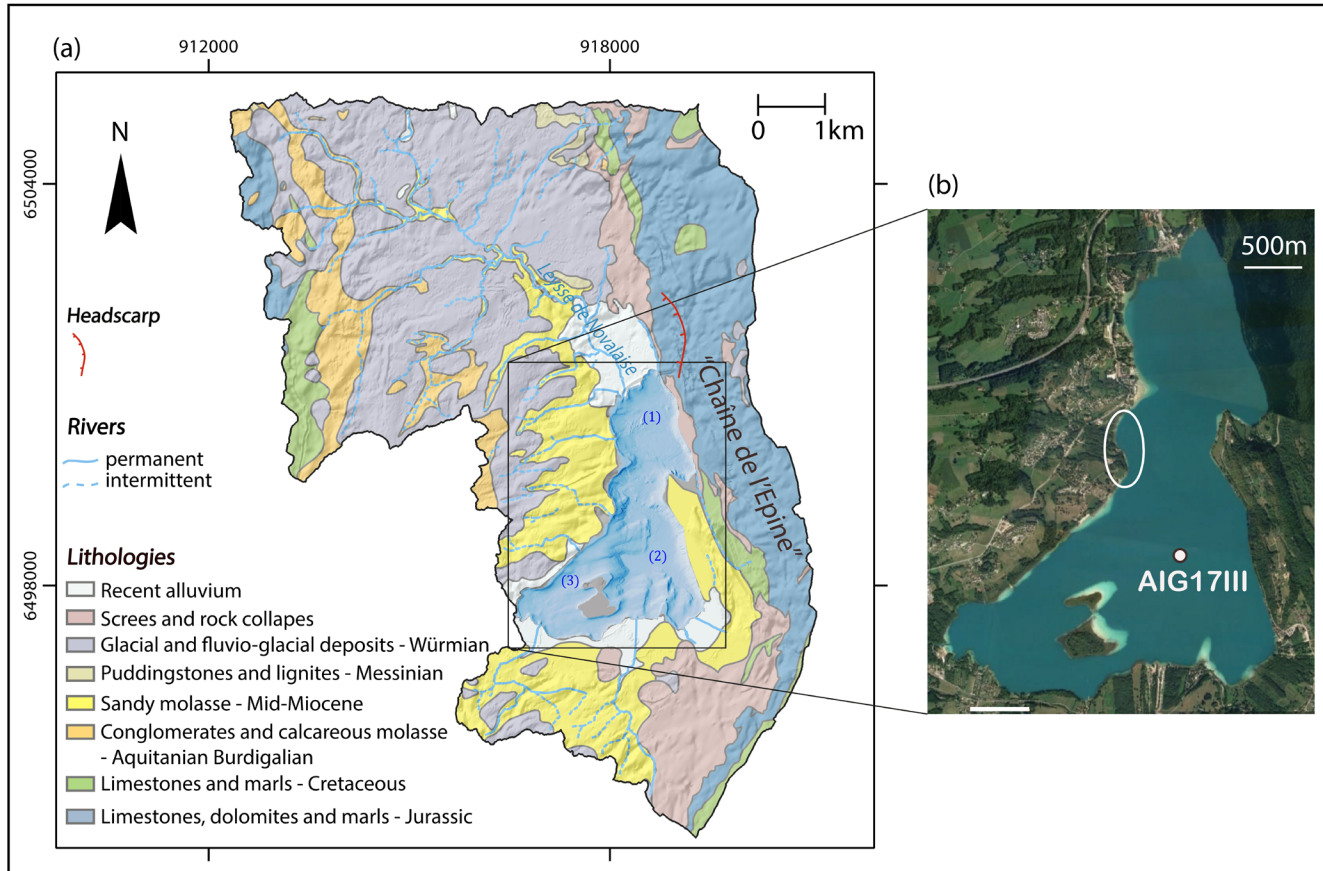


Figure 1. (a) Geological map of the Lake Aiguebelette catchment with the three subbasins of the lake: (1) northern basin, (2) deep basin and (3) shallow southern basin. (b) Depicts the core site of the AIG17III sediment sequence in the deep basin (shown in Fig. 2). The white circle on the lake's western shore shows the sliding mass position. We can observe the littoral carbonate platform on the western coast in light blue, except for the area of sliding mass in the white circle (modified from Banjan et al. (2022)).

Banjan et al. (2022) present a high-resolution bathymetric survey along with the seismic and core data acquisition, which allows for the identification of large mass wasting deposits. A bathymetric survey was carried out using a Reson 8101 multibeam echo-sounder (Teledyne Reson, Slangerup, Denmark) in October 2017 and processed with QINSy 8.15.0 software (QPS, The Netherlands). Prior to seismic data acquisition, a 16 m-long core named AIG17III collected in 2017 using a Uwitec platform and corers (Uwitec, Mondsee, Austria) belongs to the deep basin of Lake Aiguebelette (45.5503°N, 5.8015°E) at a depth of 70 meters (Fig. 2a(iv)). The seismic data (Fig. 2a(i)) was collected in 2020 using an Echoes 10,000 chirp subbottom profiler and processed with Delph Seismic software (iXblue, Saint-Germain en Laye, France). For more details, see Banjan et al. (2022).

These seismic profiles and core data provide detailed information about the event layer in the deep basin. Seismic stratigraphy (Fig. 2a(iii)) was interpreted based on the correlation between AIG17III sequence

units and thickness obtained from seismic profiles. The interpretation is as follows: LU (Lower Unit) refers to sediments that have been deposited during the Late Glacial. MU (Middle Unit) corresponds to an event layer at the YD–EH transition, and an upper unit (UU) which represents the Holocene sediments. A seismic survey shown in Fig. 2a(i) enabled Banjan et al. (2022) to determine the thickness of the final mass-transport deposits (Fig. 2b) ranging from 0.6 m to 1.7 m in areas that are not gas blind.

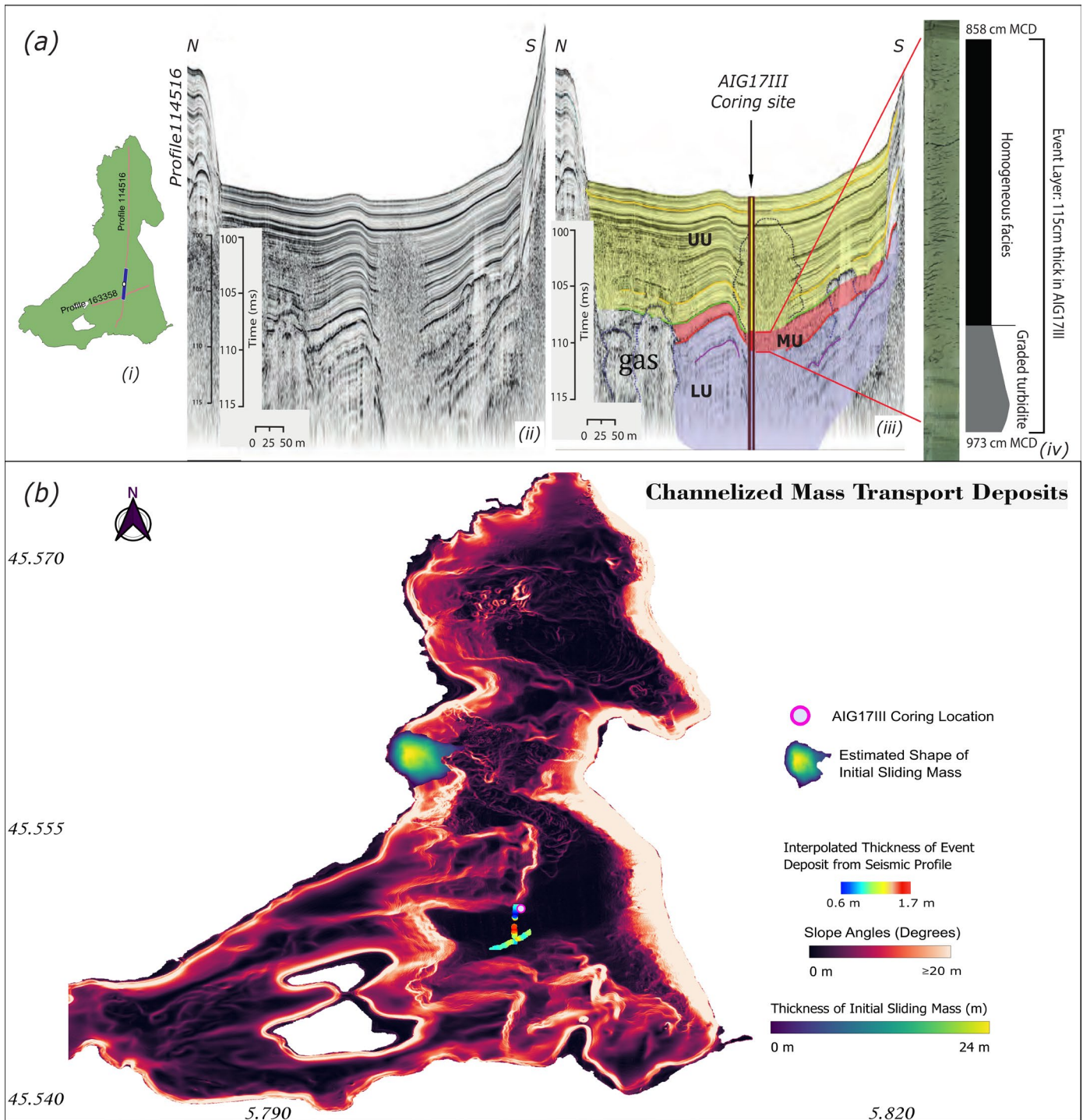


Figure 2. a(i) Displays seismic profiles 114516 and 163358 within the lake. Parts of these lines highlighted in blue correspond to the sections shown in a(ii) and a(iii). A dot marks the location of the sediment core sample. a(ii) Shows the uninterpreted section of the seismic profile highlighted in a(i). Interpretation of the seismic profile with lower (LU), middle (MU) and upper (UU) seismic units along with sediment core AIG17III are presented in a(iii). 115 cm thick event layer in the AIG17III sedimentary sequences can be shown in a(iv). (b) Shows the map of channelized mass transport deposits and slope angles which includes overlays of the shape and thickness of the initial sliding mass and the interpolated thickness derived from seismic profiles (modified from Banjan et al. (2022)).

Additionally, core data allowing the characterization of a 115 cm thick turbidite–homogenite (Fig. 2a(iv)), which was dated to 11,700 yr cal BP, corresponding to the YD-EH climatic transition. In Fig. 2b, the channelized mass transport deposits indicate that mass deposits come from an area on the western flank of the lake, where coastal carbonate platforms are absent (Fig. 1b). However, littoral carbonates are seen everywhere on the western side of the lake, except where the channelized morpho-bathymetric feature arises (Fig. 1b). The initial sliding mass was therefore identified on the western shore of the lake by mapping sediment head traces through GIS analysis of bathymetric data (Fig. 2b). By reconstructing a prefailure slope profile on the bathymetric data, the volume of this mass transport deposit is estimated to be approximately 767000 m^3 using kriging interpolation, the shape of the initial mass with thickness are shown in Fig. 2b. Analysis of core sediments enabled the identification of an average wet density of 1600 kg/m^3 , corresponding to approximately 11,700 years ago. For a representation of these density variations over time, refer to the graph in Supplementary figure (S1). The detailed characteristics of the initial sliding mass along with maximum and mean values of physical parameters are shown in Table 1.

*Table 1. Physical characteristics of initial sliding mass; *indicating final deposit values, D50 and D90 represent the median and 90th percentile diameters of the particles, respectively.*

Max thickness	24 m	Mean thickness	11 m
Max length	300 m	Mean length	240 m
Max density	1700 kg/m^3	Mean density	1600 kg/m^3
Coarser D50 grain size*	$250\text{ }\mu\text{m}$	Coarser D90 grain size*	$500\text{ }\mu\text{m}$
Fine D50 grain size*	$6\text{ }\mu\text{m}$	Fine D90 grain size*	$30\text{ }\mu\text{m}$
Max slope (°)	30	Mean slope (°)	11

3 Numerical Models Used in This Study

3.1 Mass Movement Model

Sublacustrine mass movements involve complex layered structures, including a dense bottom debris layer covered by a thin layer entrained by turbidity currents (Liapidevskii et al., 2018, Liapidevskii and Dutykh, 2019). This bottom layer can be taken as either a clay-rich visco-plastic flow or a granular, incoherent flow. There will be no deformation in the case of viscoplastic flow unless the shear stress exceeds the yield strength. When it exceeds this limit, the flow begins to behave as a shear-thinning, non-Newtonian fluid. This type of flow behavior is taken as Herschel-Bulkley rheology, which is incorporated herein applied numerical depth-averaged mass transport model called BingClaw (Kim, 2020a), modified from (Huang & García, 1997; Imran et al., 2001).

The Herschel-Bulkley rheological model for simple shear can be defined as follows:

$$|\dot{\gamma}/\dot{\gamma}_r|^n = \begin{cases} \text{sgn}(\dot{\gamma}) \left((\tau/\tau_y) - 1 \right), & \text{if } |\tau| > \tau_y, \\ 0, & \text{otherwise,} \end{cases}$$

where τ and τ_y are the shear stress and yield strength, respectively, $\dot{\gamma}$ is the strain rate and $\dot{\gamma}_r$ is the reference strain rate, given as

$$\dot{\gamma}_r = \left(\frac{\tau_y}{\mu} \right)^{\frac{1}{n}}.$$

The model integrates the mass balance equations over the entire flow depth and solves the momentum equations separately for the top plug layer, which exhibits no shear deformation, and the bottom shear layer. The entire flow depth is shown as $H = H_s + H_p$. Here, H_p and H_s represent the thickness of the plug and the shear layers in the vertical direction, respectively. Volumetric flux through the plug ($H_p \mathbf{u}_p$) and the shear layers ($H_s \mathbf{u}_s$) with velocities \mathbf{u}_p and \mathbf{u}_s parallel to the slope within the plug and the shear layer, respectively:

$$\begin{aligned} & \frac{\partial}{\partial t}(H_p + H_s) + \nabla \cdot (H_p \mathbf{u}_p + H_s \mathbf{u}_s) = 0, \\ & \left(1 + C_m \frac{\rho_w}{\rho_d}\right) \frac{\partial}{\partial t}(H_p \mathbf{u}_p) + \nabla \cdot (H_p \mathbf{u}_p \mathbf{u}_p) + g' H_p \nabla (H_p + H_s + b) + \mathbf{u}_p \left(\frac{\partial}{\partial t} H_s + \right. \\ & \quad \left. \nabla \cdot (H_s \mathbf{u}_s) \right) = - \frac{\mathbf{u}_p}{\|\mathbf{u}_p\|} \frac{\tau_y + \tau_d}{\rho_d}, \\ & \left(1 + C_m \frac{\rho_w}{\rho_d}\right) \frac{\partial}{\partial t}(H_s \mathbf{u}_s) + \nabla \cdot (\alpha H_s \mathbf{u}_s \mathbf{u}_s) + g' H_s \nabla (H_p + H_s + b) \\ & \quad - \mathbf{u}_p \left(\frac{\partial}{\partial t} H_s + \nabla \cdot (H_s \mathbf{u}_s) \right) = - \frac{\mathbf{u}_p}{\|\mathbf{u}_p\|} \frac{\tau_y f_s}{\rho_d}. \end{aligned}$$

This depth-averaged model operates in 2HD (or two horizontal dimensions), and all vector quantities along with the nabla operator ∇ are two-dimensional horizontal directions. Here, $b(x, y)$ represents the bathymetry, C_m is the added-mass coefficient, ρ_w and ρ_d are the density of ambient water and the landslide, respectively, α is the velocity form factor in the shear layer, and t is the time coordinate. The reduced gravitational acceleration (considering the buoyancy effects) is defined as $g' = g(1 - \rho_w - \rho_d)$. The term in the momentum equations $g' H_{ps} \nabla (H + b)$ merges the slope parallel component of gravity and the pressure gradient. The viscous drag on the free surface represented by τ_d , which is divided into friction drag τ_f and a pressure drag term τ_p , given as:

$$\tau_f = \frac{1}{2} C_F \rho_w \mathbf{u}_p \|\mathbf{u}_p\|, \quad \tau_p = \frac{1}{2} C_P \rho_w \max(0, -\mathbf{u}_p \cdot \nabla H) \mathbf{u}_p,$$

where C_F and C_P represent the hydrodynamic coefficients of friction and pressure drags, respectively. On the right-hand side of the share-layer momentum balance, $\tau_y f_s$ represents the net shear stress at the bed. Here,

$$f_s = \beta \cdot \left(\frac{\|\mathbf{u}_p\|}{\dot{\gamma}_r H_s} \right)^n,$$

with shape factor $\beta = \left(1 + \frac{1}{n}\right)^n$.

In BingClaw, dominant advective terms are modeled using finite volume and source terms by finite difference methods. This framework utilizes the numerical conservation law package ClawPack (Mandli et al., 2016). In computational grids where the pressure gradient together with gravity $\rho_d g' H_{ps} \nabla (H + b)$ does not exceed the material shear strength, the cell remains static. If it does, the dynamic equations are solved using the Godunov-type fractional step method. ClawPack first solves the equations without friction terms using the finite volume method and then accounts for frictional terms in the next fractional step. For a more detailed derivation, see Kim et al. (2019).

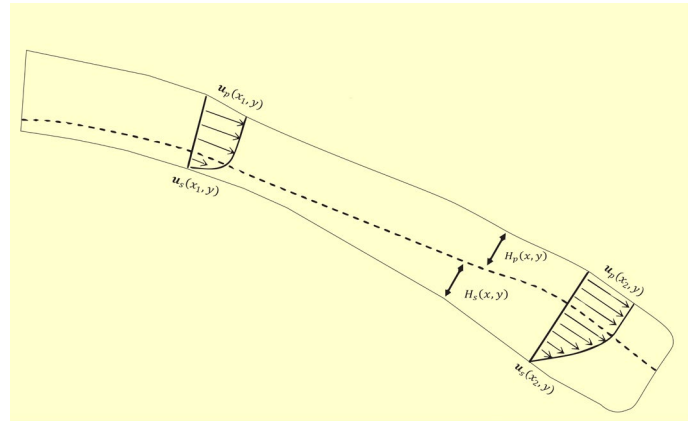


Figure 3. Velocity profile in a depth-averaged Herschel-Bulkley fluid model. The velocity within the top plug layer is uniform, while in the shear layer it follows a power law with an exponent of $n+1$, characteristic of shear-thinning non-Newtonian behavior. The figure illustrates how the thicknesses and velocities of both the plug and shear layers can spatially vary with respect to the x and y coordinates.

3.2 Tsunami Models

3.2.1 Nonlinear Shallow Water Model

We use the GeoClaw model (ClawPack Development Team, 2020), a version of the Clawpack that is a set of numerical methods for solving nonlinear hyperbolic conservation laws. GeoClaw solves the two-dimensional depth-averaged nonlinear shallow water equations using well-balanced Godunov-type finite volume schemes (Godunov & Bohachevsky, 1959; Toro, 2001; LeVeque, 2002) on rectangular grids. It solves corresponding Riemann problem at each cell interface and allows the discontinuous solution or shock wave that arises in hyperbolic PDEs. The Riemann problem (Godunov & Bohachevsky, 1959) consists of the specified equations (NSWE) combined with piecewise constant initial data determined by the cell averages on either side. Additionally, we can incorporate adaptive mesh refinement for robust and efficient solutions for large-scale geophysical problems, and it captures wet–dry interfaces efficiently for inundation modeling. For a detailed description of GeoClaw, see LeVeque et al. (2011). We used the temporal volumetric moving bathymetry resulting from the mass-movement model BingClaw as input for tsunami generation and computed the tsunami propagation and inundation for the Lake Aiguebelette.

3.2.2 Dispersive Boussinesq Model

When discussing the genesis of tsunami events triggered by landslides, the concept of dispersion is an essential factor to consider. We applied a dispersive tsunami model called “BousClaw” (Kim, 2020b) developed in the framework of the modified Boussinesq equations suggested by Schäffer et al. (1993) and Schäffer and Madsen (1995). BousClaw integrates the dispersion terms only for the momentum equation to simplify the model and retains accurate dispersion characteristics for shorter-wavelength waves. The conservative Boussinesq equations are divided into two principal components using the operator-splitting approach: the shallow water equations and the dispersive terms. Initially, the model solves the shallow water equations employing a high-resolution finite volume scheme and then solves the dispersion terms using a finite difference scheme. To account for wave breaking, we implement a criterion based on the wave height to water depth ratio. When this ratio exceeds 0.8, the model automatically switches to the standard set of shallow water equations, thereby capturing the wave dynamics more realistically. A more exhaustive treatment of the underlying equations and numerical techniques is available in Kim et al. (2017). The results for the mass movement and tsunami models are presented in the following section.

4 Results

4.1 Mass Movement Simulations

The volume and shape of the displaced mass are estimated by kriging interpolation using the current bathymetry due to insufficient information on the pre-failure bathymetry. However, with the help of geological and seismic data, the comparison of the simulation results with the observations provides the ground for the validation of the results and leads us to a realistic volume. The range of the non-Newtonian fluidity index n is $0 < n < 1$ for shear thinning Herschel-Bulkley flow, and we used $n = 1/2$ (Løvholt et al., 2017) in the simulations. Other key parameters for the mass movement model are listed in Table 2. Since runout distance is more sensitive to yield strength (Kim et al., 2019), multiple tests are performed to choose the appropriate yield strength to maintain close agreement with paleotsunami runout

Table 2. Mass movement model parameters

Parameter	Value
Volume	767000 m^3
Rheological Model	Herschel-Bulkley
Slide Density	1600 kg/m^3
Fluid Density	1000 kg/m^3
Reference Strain Rate	100 S^{-1}
Yield Strength	60 pa
Added Mass	0.1
Frictional Drag	0.01
Pressure Force	1.0

observations. We take into account the added mass to ensure a more accurate representation of the interaction between the landslide mass and the surrounding water body. The added mass coefficient C_m for short blocks is calculated in the order of magnitude of 1 by Watts (2000). However, the added-mass coefficient C_m value depends on the ratio of the landslide thickness to length (Enet & Grilli, 2007). Considering the specific dimensions of our landslide, which suggest a relatively low thickness-to-length ratio, based on these dimensions and in line with previous studies (Kim et al., 2019; Zengaffinen et al., 2020), we have opted for a C_m value of 0.1. Typical values for the pressure force $C_p = 1.0$ and the frictional drag $C_F = 0.01$ were also considered for the simulation of mass failure to maintain realistic velocity and acceleration. By using these parameters, mass movement simulations are conducted on uniform rectangular computational grids 480×400 with 5 meters spatial resolution and by using high-resolution bathymetry data with a 2 m resolution. The simulated thickness and run-out distance of mass-movement deposits at various times are shown in Fig. 4. Mass deposits take approximately 12 min to travel to the final deposit location.

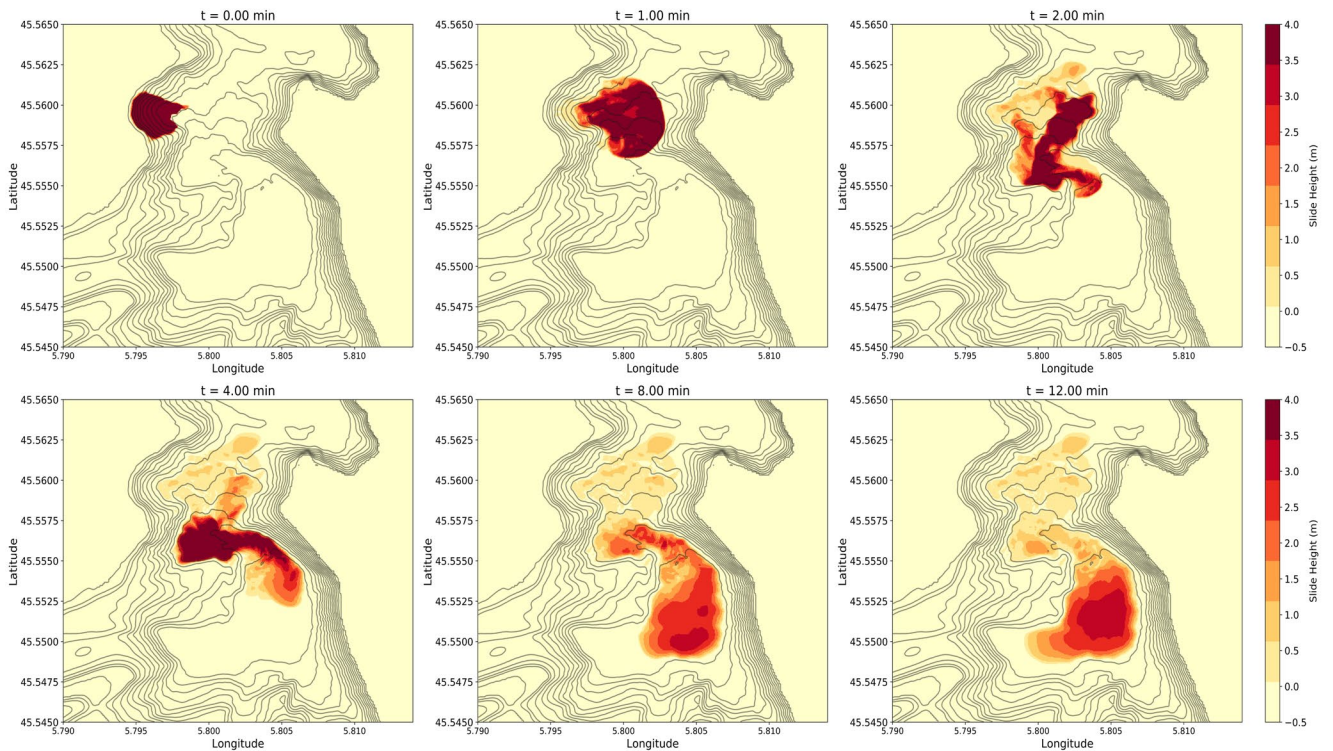


Figure 4. Snapshots of the thickness and runout distance of the mass movement numerical model results at 0, 1, 2, 4, 8, and 12 min after the destabilization

4.2 Tsunami Simulations

The primary source of tsunami generation in this study is temporal variations in the lakebed bathymetry caused by sublacustrine mass movement. Such progressive bathymetric changes are the outputs of the mass movement model, BingClaw. We included BingClaw results in the tsunami model as inputs for tsunami generation. These perturbations are directly transformed into the overlying water column and the water surface. Tsunami propagation and inundation are performed using the nonlinear shallow water equations (NSWE) and dispersive Boussinesq equations for Lake Aiguebelette by using an offshore bathymetry dataset with a resolution of 2 m and onshore high-resolution topography with 1 m resolution employed for inundation modeling. The uniform rectangular computational grids 720×600 were used with 5 m spatial resolution. The computational domain for tsunami simulations is larger than for landslide simulations, as it covers larger area, resulting in increases grid cells.

4.2.1 Wave Propagation and Inundation

The propagation of tsunami waves over time computed by both NSWE and Boussinesq models are shown in Fig. 5(a) and Fig. 5(b), respectively. Black dots represent offshore and onshore synthetic gauge numbers from 1-10 and 11-15, respectively. Upon failure of the mass, the surface amplitude is rapidly increasing to approximately 3 m initially at $t = 6$ s. After that, the leading wave propagated ~ 800 m from the landslide origin area in the direction of the sliding mass with a maximum amplitude greater than

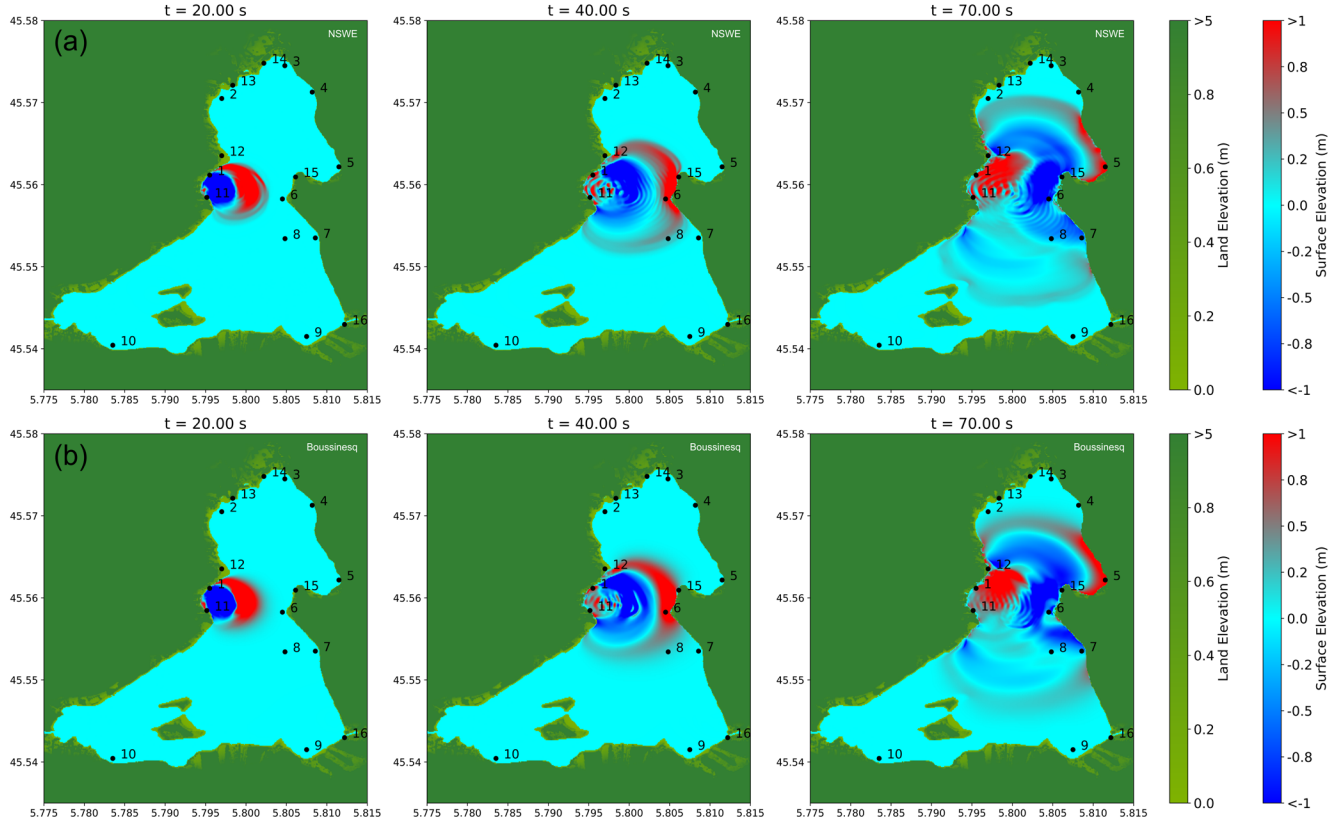


Figure 5. Wave propagation snapshots at 20, 40, and 70 seconds using NSWE (a) and Boussinesq models (b). Locations of synthetic gauges 1-15 marked with black dots.

1.5 m at $t = 30$ s and reached the opposite eastern shore, right in front of the massive subaqueous failure. After 30 s, waves propagate everywhere in the lake, but they show more development in the north-eastern quadrant. The wave propagates across the entire lake within 2 min with maximum velocity of 25 ms^{-1} , although the mass deposits reach the final deposition area in 12 min with maximum velocity 10 ms^{-1} . We can observe that this sublacustrine mass movement produced a significant tsunami wave with maximum amplitude of 3 m. Time series of water surface elevation at synthetic gauges were extracted from the tsunami simulations and are shown in Fig. 6, together with the maximum amplitude over arrival time (s) across the entire lake. Waves of approximately 2 m amplitude are observed near the source on Gauge 1 and 1.4 m near the opposing shore on Gauge 6 in the direction of the leading wave (Fig. 6b). The amplitude at the lake's deepest basin is approximately 0.4 m on Gauge 8. In Fig. 6a, we can observe maximum amplitudes throughout the lake, with higher amplitudes in lake's center in the east-west direction.

The amplitude time series appears similar in both models, and the dispersion effect is less important for this event (see the Discussion section for more details). Consequently, we have chosen to model the runup height using only the NSWE model. Inundation modeling is conducted on finer grids by using the current topography data of the lake shore to observe the effects of tsunami waves at nearby shores. The tsunami runup with synthetic gauges 11-15 at onshore locations can be observed in Fig. 7.

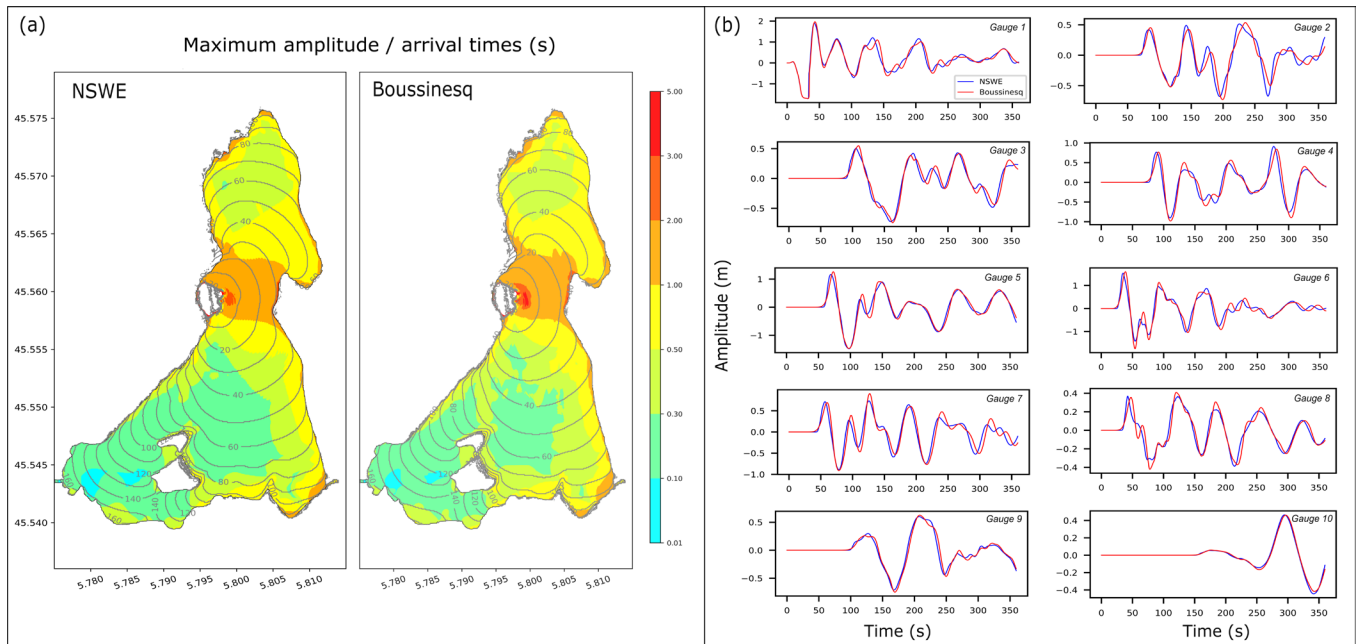


Figure 6. Maximum wave amplitude across the lake over time from 0 to 360 sec (a) with time series of wave amplitude at synthetic gauges 1-10 at offshore locations (b).

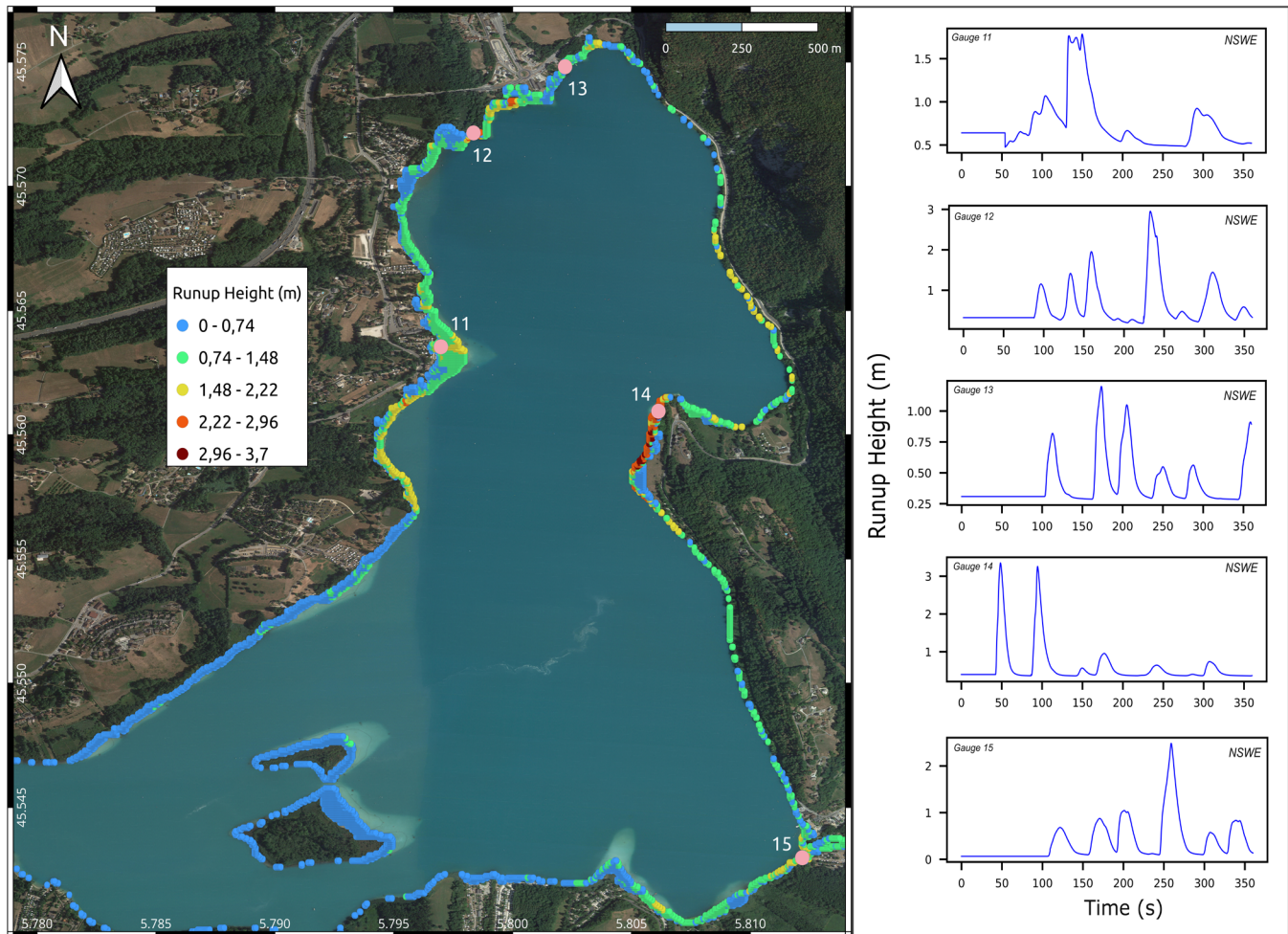


Figure 7. Runup height (left) and time series of runup heights at the indicated synthetic gauges 11-15 (right) across the lake shore, bearing in mind the present-day bathymetry and shoreline.

The topography surrounding the lake features significantly steeper slopes on the east side of the lake, which is a mountain area. Hence, we do not observe the significant runout distance by using the current topography data. The west shore has the highest tsunami runup distance of approximately 150 m and a maximum tsunami runup height of 3.7 m.

4.2.2 Froude Number Estimation

The initiation of tsunamis is primarily determined by landslide volume and frontal area. However, the characteristics and intensity of tsunami waves and their interaction with the underwater landslide are also greatly affected by the Froude number (Fr) (Løvholt et al., 2020). The Froude number, which is defined as the ratio of the landslide's velocity to the speed of longwave gravity waves, is given by:

$$Fr = U/\sqrt{gh}.$$

Here $U := \sqrt{u^2 + v^2}$ represents the landslide's velocity magnitude. The symbols ' g ' and ' h ' denote the gravitational acceleration and the depth of the water, respectively. The Froude number remains below unity for scenarios involving purely subaqueous slides with a density below 2000 kg/m^3 (Fine et al., 2003). We calculated the maximum landslide velocity and the concurrent tsunami speed at each second to determine the Froude number evolution through time. This sublacustrine landslide falls into subcritical conditions with a maximum Froude number of 0.52; see Fig. 8. Furthermore, we noted that the peak tsunami amplitude time (Fig. 6b) corresponded to the time of the maximum Froude number. Synthetic gauges 1 and 6, where the tsunami wave was reached in the first 50 s, recorded higher wave amplitudes. This correlation between the maximum tsunami amplitude and the peak Froude number indicates that the significant energy transfer from this slide into surface waves results in the most efficient tsunami generation at the maximum Froude number, consistent with previous studies (Ward, 2001; Fine et al., 2003; Løvholt et al., 2020).

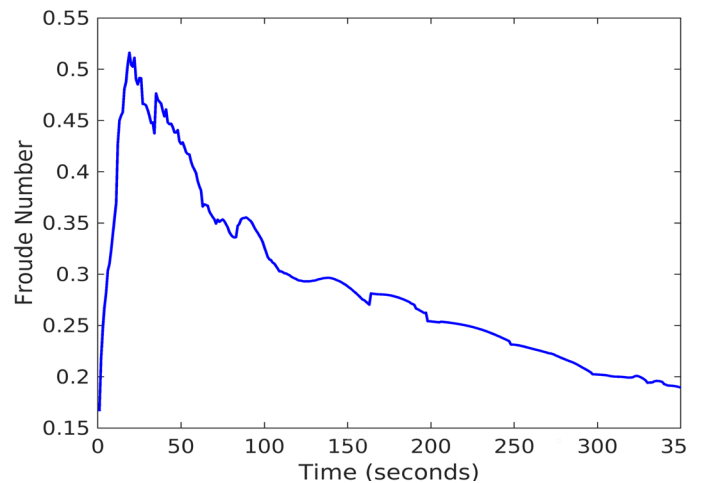


Figure 8. Variation of Froude number over time

5 Discussion

5.1 Validation of the Mass Movement Model

Simulating sublacustrine mass movement numerically provides insight into past events, allows the reconstruction of paleo events, and helps to understand the potential future hazards. Simulations of such sublacustrine landslides are complex because of their dynamic nature. Tsunamis generated by underwater landslides highly depend on the characteristics of the initial sliding mass and bathymetry (Watts, 1998; Harbitz et al., 2006; Lovholt et al., 2015). In this study, the post bathymetry data serve as our foundation. We acknowledge that substantial bathymetric changes may have occurred over the last 11,700 years, introducing uncertainties to the initial sliding mass and bathymetry. Good observation data can constrain the uncertainties. Bathymetry surveys and sediment analyses of Lake Aiguebelette provide detailed information about the initial failure mass and physical parameters such as density, water content, and sediment grain sizes from paleo-sublacustrine mass movement. Multiple tests are conducted to constrain yield strength, which is crucial to determining runout distance (Kim et al., 2019). We observed that decreasing yield strength significantly reduced runout distance, and vice versa. Based on extensive tests, we set the yield strength to 60 Pa which agrees well with the observed runout distance. Seismic and

sedimentological data enabled us to validate our mass movement model and reduced the error between the mass-movement simulations and the geological observations. Based on the parameters given in Table (1), our numerical simulations align well with the observation of the Younger Dryas – Early Holocene event. Robust agreement was found, and we obtained the same sediment thickness and runout distances derived from seismic profiles, sediment core data and numerical simulation at the final deposit location, as illustrated in the Fig. 9. Due to the remarkable agreement between the computed results and the observations, we are confident that the mass movement simulations can be used to identify the potential tsunami at the Lake Aiguebelette.

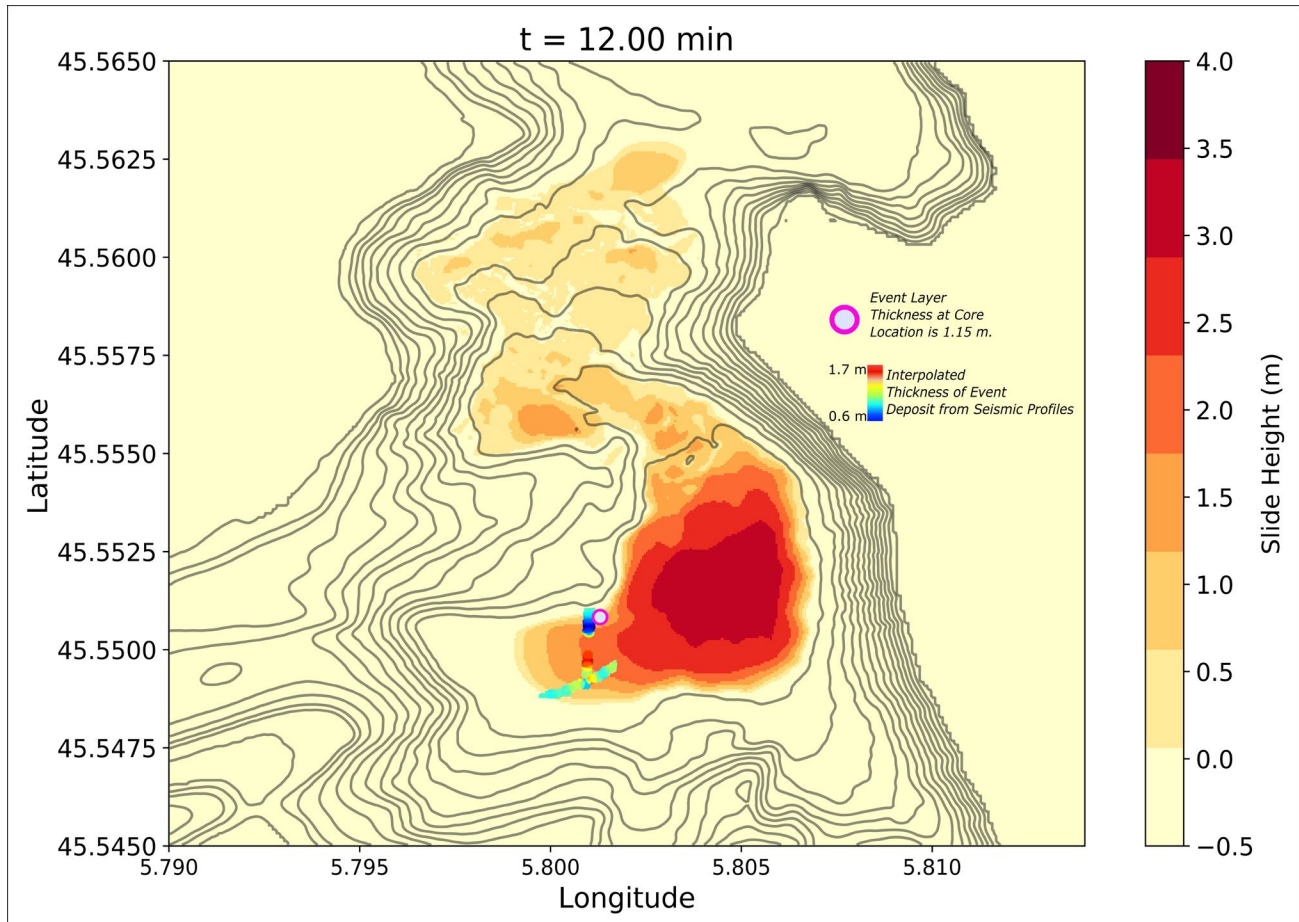


Figure 9. Validation of the estimated deposit thickness from numerical model BingClaw by comparison with event deposit thicknesses from seismic profiles and core data at the final deposition location.

5.2 Tsunami Wave Directivity

Using the well-constrained mass movement model, our investigation showed that seismically induced mass movement resulted in significant paleotsunami waves in the Lake Aiguebelette. We can observe from the mass movement propagation (Fig. 4) and wave propagation (Fig. 5) that the direction of the leading tsunami wave toward the east follows the direction of the mass deposits in the early stages of the collapse. However, over time, the speed of the mass deposits diminishes, and its influence on the tsunami wave direction becomes less pronounced in the deceleration phase. It is interesting to observe that all simulated mass transport is directed toward the south after 1.5 min, but the majority of the leading wave moves toward the east and the north. It seems that tsunami wave direction is determined by the initial phase of mass-movement deposits and the bathymetry features of the area. Since tsunami wave direction is essential for locating potential tsunami deposits, the results of this numerical study provide insight into potential paleotsunami deposit locations. Eventually, we intend to locate the tsunami deposits in the

direction of the highest positive wave to gain a deep understanding of this paleo-sublacustrine tsunami event. It is crucial to note that we simulate the tsunami event that occurred approximately 11,700 years ago, even though water levels fluctuated over time, while this variation in water levels might influence our findings. Regarding tsunami hazards in this area, we performed calculations for the run-up distance and height by using the current topography, as shown in Fig. 7. The most affected area is along the western side of the lake because it is less steep than the eastern shore, although the run-up height is greater at the eastern shore. The run-up is mainly dependent on the local bathymetric features close to the shoreline (e.g., Grilli et al., 2009; De Blasio 2011). Overall, we do not obtain a significant runup distance because the steep slope confines the inundation process. Additionally, the limited energy of the tsunami associated with the small volume of the slide also contributes to the rapid attenuation of the wave, further reducing the runup distance.

5.3 Dispersion Analysis

In this section, we analyze the numerical results obtained from the hydrostatic, nondispersive NSW model and the weakly dispersive Boussinesq model to estimate the influence of frequency dispersion on tsunami waveforms. Notably, the tsunami wave propagations (Fig. 5) and time series waveforms (Fig. 6) do not predispose the dispersion; the amplitude and arrival time of the first wave appears to be quite similar for both models and do not show secondary short waves. There is a striking similarity between the waveforms produced by the non-dispersive and Boussinesq models. These results indicate that waveforms remain under the long wave assumptions $depth \ll wavelength$ throughout propagation, and dispersion is unimportant for this event, even though it was generated by an underwater landslide.

To illustrate this behavior, we plotted the amplitude as a distance function to analyze the wavelength. We made spatial cuts along wave propagation at times 27 s and 50 s and attempted to capture the wavelength of the lake with a relatively small spatial lake scale. We found that the longest wavelength reached approximately 1.5 km, 22 times greater than the maximum water depth of 70 m. The wavelength graphs at 27 s in the east–west direction (frontal area) can be seen in Fig. 10a, and those at 50 s in the north–south direction are shown in Fig. 10b. We also calculated other parameters, including *non-linearity* ≈ 0.07667 , *dispersion* ≈ 0.00071 , and the *Stokes-Ursell number* ≈ 107.23827 , to assess the impact of dispersion on the lake's wave dynamics. These results show that the wavelength was much greater than the water depth, and the wave was nonlinear and nondispersive in this context.

6 Conclusions

In this paper, we modeled the mass movement and corresponding tsunami in Lake Aiguebelette using a viscoplastic Herschel-Bulkley rheological model coupled in one way with the hydrodynamic nonlinear shallow water equations and the dispersive Boussinesq equations. This research study provides evidence for the potential for significant sublacustrine mass movement-induced paleotsunami in this alpine lake. Our numerical simulations shed light on tsunami characteristics and its dynamics. We analyze how paleo-sublacustrine mass movement in a lake environment may lead to tsunamis. Using detailed geologic and bathymetric data, we simulated the thickness and runout distance of mass movement deposits over time, and the simulations are in excellent alignment with geophysical observations. For the tsunami simulations, we determine that the sublacustrine mass movement with an estimated initial volume of

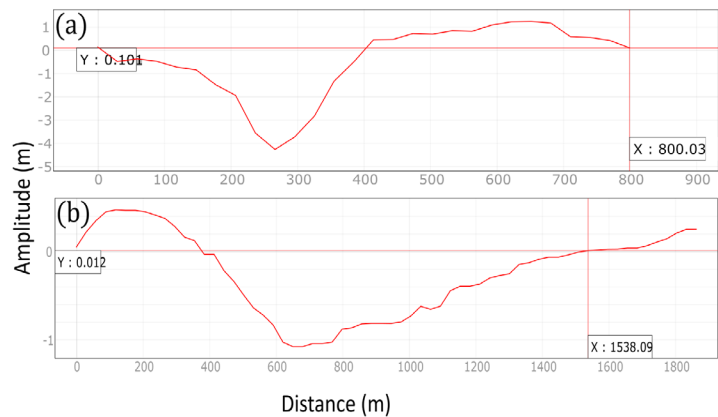


Figure 10. Wavelength at 27 s in east–west direction (a) and wavelength at 50 s in the north–south direction (b).

767000 m^3 could have transported enough sediments to generate a basin-wide tsunami in Lake Aiguebelette with a maximum of 3.7 m runup height, but with relative short inundation distance in relation to high topographic variations. Tsunami simulations show that the amplitude of the tsunami wave in the east–west direction is approximately 1 – 3 m, which causes a substantial tsunami. We conducted a comparative study between the NSW and dispersion models to observe the importance of dispersion effects in small-scale lacustrine environments. We observed that dispersion has little importance in this event; wave propagation snapshots and wave amplitude time series appear similar. This multidisciplinary research is key to understanding the past event that occurred in the Younger Dryas–Early Holocene climatic transition and, if such an event occurred in the future climate change, how it could impact the lake shore.

Acknowledgements

We thank the Conservatoire des Espaces Naturels de Savoie, CCLA and Réserve Naturelle Régionale du Lac d’Aiguebelette for bathymetric data. We are grateful to iXBlue for their help in acquiring seismic reflection data and providing access to DELPH interpretation software. We thank Erwan Messenger, Christian Crouzet, and Hervé Jomard for their work and support in the PhD of Mathilde Banjan on sediment cores from Aiguebelette Lake. We thank Xavier Bodin for his help in the use of GIS software. This publication is based upon work supported by the Khalifa University of Science and Technology under Award No. FSU-2023-014. MNZ gratefully acknowledges the financial support received from the MESRI and ED MSTII in the form of a PhD scholarship to conduct research for his doctoral thesis.

Data Availability Statement

In this study, we used three open-source softwares for numerical simulations. The mass movement model BingClaw (Kim, 2020a) is available at the GitHub repository <https://github.com/jhkim2/BingClaw>. The non-dispersive model GeoClaw (ClawPack Development Team, 2020) can be found at <https://www.clawpack.org/geoclaw>. The weakly dispersive model BoussClaw (Kim, 2020b) is accessible at the GitHub repository <https://github.com/jhkim2/BoussClaw>. The simulation data (Zafar et al., 2023) generated from these three models are made accessible under the Creative Commons Attribution Share Alike 4.0 International license in the Zenodo repository <https://zenodo.org/doi/10.5281/zenodo.10426254>. This repository contains all the output files and scripts necessary to run and reproduce our simulation results.

References

- Abe, K. (1973). Tsunami and mechanism of great earthquakes. *Physics of the earth and planetary interiors*, 7(2), 143-153.
- Abe, T., Goto, K., & Sugawara, D. (2012). Relationship between the maximum extent of tsunami sand and the inundation limit of the 2011 Tohoku-Oki tsunami on the Sendai Plain, Japan. *Sedimentary Geology*, 282, 142–150.
- Assier-Rzadkiewicz, S., Heinrich, P., Sabatier, P.C., Savoye, B., & Bourillet, J.F. (2000). Numerical modeling of a landslide-generated tsunami: the 1979 Nice event. *Pure and Applied Geophysics*, 157, 1707–1727.
- Banjan, M., Crouzet, C., Sabatier, P., Jomard, H., Bajard, M.J.A., Demory, F., Develle, A-L, Jenny, 440 J.P., Fanget, B., Malet, E., Findling, N., Alain, P., Didier, J., Bichet, V., Clapot, S., and 441 Messenger, E. 2022. Did the Younger Dryas to Holocene climate transition favor high seismicity 442 rates in the northwestern Alps?. *Sedimentology*, 70(2), pp.538-568.
- Bardet, J. P., Synolakis, C. E., Davies, H. L., Imamura, F., & Okal, E. A. (2003). Landslide tsunamis: Recent findings and research directions. *Pure and Applied Geophysics*, 160, 1793-1809.

- Beck, C. (2009). Late Quaternary lacustrine paleo-seismic archives in northwestern Alps: Examples of earthquake-origin assessment of sedimentary disturbances. *Earth-Science Reviews*, 96(4), 327–344.
- Behrens, J., Løvholt, F., Jalayer, F., Lorito, S., Salgado-Gálvez, M.A., Sørensen, M., Abadie, S., Aguirre-Ayerbe, I., Aniel-Quiroga, I., Babeyko, A. and Baiguera, M. (2021). Probabilistic tsunami hazard and risk analysis: A review of research gaps. *Frontiers in Earth Science*, 9, p.628772.
- Beigt, D., Villarosa, G., Gómez, E. A., & Manzoni, C. (2016). Subaqueous landslides at the distal basin of Lago Nahuel Huapi (Argentina): Towards a tsunami hazard evaluation in Northern Patagonian lakes. *Geomorphology*, 268, 197-206.
- Beizel, S. A., Chubarov, L. B., Dutykh, D., Khakimzyanov, G. S., & Shokina, N. Y. (2012). Simulation of surface waves generated by an underwater landslide in a bounded reservoir. *Russian Journal of Numerical Analysis and Mathematical Modeling*, 27(6), 539-558.
- Biguenet, M., Sabatier, P., Chaumillon, E., Chagué, C., Arnaud, F., Jorissen, F., Coulombier, T., Geba, E., Cordrie, L., Vacher, P. and Develle, A.L. (2021). A 1600 year-long sedimentary record of tsunamis and hurricanes in the Lesser Antilles (Scrub Island, Anguilla). *Sedimentary Geology*, 412, 105806.
- Blikra, L. H., Nemeč, W., & Harbitz, C. B. (2005). Quantification of rock-avalanche and tsunami hazard in Storfjorden, western Norway. In *Landslides and avalanches* (pp. 57–64). ICFL.
- Bondevik, S., Svendsen, J. I., Johnsen, G., Mangerud, J. A. N., & Kaland, P. E. (1997). The Storegga tsunami along the Norwegian coast, its age and run up. *Boreas*, 26(1), 29-53.
- Bosa, S., & Petti, M. (2011). Shallow water numerical model of the wave generated by the Vajont landslide. *Environmental Modelling & Software*, 26(4), 406-418.
- Bussmann, F., and Anselmetti, F. S. (2010). Rossberg landslide history and flood chronology as recorded in Lake Lauerz sediments (Central Switzerland). *Swiss J. Geosci.* 103, 43–59. doi:10.1007/s00015-010-0001-9
- Chagué-Goff, C., Szczuciński, W., & Shinozaki, T. (2017). Applications of geochemistry in tsunami research: A review. *Earth-Science Reviews*, 165, 203-244.
- Chapron, E., Beck, C., Pourchet, M., & Deconinck, J. F. (1999). 1822 earthquake-triggered homogenite in Lake Le Bourget (NW Alps). *Terra Nova*, 11(2-3), 86–92.
- Clawpack Development Team. (2020). Clawpack [Software]. Retrieved from <https://www.clawpack.org/geoclaw>.
- Cordrie, L., Feuillet, N., Gailler, A., Biguenet, M., Chaumillon, E., & Sabatier, P. (2022). A Megathrust earthquake as source of a Pre-Colombian tsunami in Lesser Antilles: Insight from sediment deposits and tsunami modeling. *Earth-Science Reviews*, 228, 104018.
- Dan, G., Sultan, N., & Savoye, B. (2007). The 1979 Nice harbor catastrophe revisited: trigger mechanism inferred from geotechnical measurements and numerical modeling. *Marine Geology*, 245(1-4), 40-64.
- De Blasio, F. V. (2011). Subaqueous Landslides. *Introduction to the Physics of Landslides: Lecture notes on the dynamics of mass wasting*, 295-351.
- Dias, F., Dutykh, D., O'Brien, L., Renzi, E., & Stefanakis, T. (2014). On the modeling of tsunami generation and tsunami inundation. *Procedia IUTAM*, 10, 338-355.
- Dutykh, D., & Dias, F. (2007). Water waves generated by a moving bottom. In *Tsunami and Nonlinear waves* (pp. 65-95). Berlin, Heidelberg: Springer Berlin Heidelberg.
- Dutykh, D., & Kalisch, H. (2013). Boussinesq modeling of surface waves due to underwater landslides. *Nonlinear Processes in Geophysics*, 20(3), 267-285.
- Dutykh, D., Dias, F., & Kervella, Y. (2006). Linear theory of wave generation by a moving bottom. *Comptes Rendus Mathématique*, 343(7), 499-504.
- Dutykh, D., Mitsotakis, D., Beisel, S. A., & Shokina, N. Y. (2013). Dispersive waves generated by an underwater landslide. In E. Vazquez-Cendon, A. Hidalgo, P. Garcia-Navarro, & L. Cea (Eds.),

- Numerical Methods for Hyperbolic Equations: Theory and Applications (pp. 245-250). CRC Press.
- Enet, F., & Grilli, S. T. (2007). Experimental study of tsunami generation by three-dimensional rigid underwater landslides. *Journal of Waterway, Port, Coastal, and Ocean Engineering*, 133(6), 442-454.
- Fanetti, D., Anselmetti, F. S., Chapron, E., Sturm, M., & Vezzoli, L. (2008). Megaturbidite deposits in the Holocene basin fill of Lake Como (southern Alps, Italy). *Palaeogeography, Palaeoclimatology, Palaeoecology*, 259(2-3), 323-340.
- Fine, I. V., Rabinovich, A. B., Thomson, R. E., & Kulikov, E. A. (2003). Numerical modeling of tsunami generation by submarine and subaerial landslides. *Submarine landslides and tsunamis*, 69-88.
- Girardclos, S., Schmidt, O. T., Sturm, M., Ariztegui, D., Pugin, A., & Anselmetti, F. S. (2007). The 1996 AD delta collapse and large turbidite in Lake Brienz. *Marine Geology*, 241(1-4), 137-154.
- Godunov, S. K., & Bohachevsky, I. (1959). Finite difference method for numerical computation of discontinuous solutions of the equations of fluid dynamics. *Matematičeskij sbornik*, 47(3), 271-306.
- Goto, K., Chagué-Goff, C., Fujino, S., Goff, J., Jaffe, B., Nishimura, Y., Richmond, B., Sugawara, D., Szczuciński, W., Tappin, D.R. and Witter, R.C. (2011). New insights of tsunami hazard from the 2011 Tohoku-oki event. *Marine Geology*, 290(1-4), 46-50.
- Goto, T., Satake, K., Sugai, T., Ishibe, T., Harada, T., & Gusman, A. R. (2019). Tsunami history over the past 2000 years on the Sanriku coast, Japan, determined using gravel deposits to estimate tsunami inundation behavior. *Sedimentary Geology*, 382, 85-102.
- Grilli, S. T., Taylor, O. D. S., Baxter, C. D., & Marezki, S. (2009). A probabilistic approach for determining submarine landslide tsunami hazard along the upper east coast of the United States. *Marine Geology*, 264(1-2), 74-97.
- Hampton, M. A., Lee, H. J., & Locat, J. (1996). Submarine landslides. *Reviews of geophysics*, 34(1), 33-59.
- Harbitz, C. B., Løvholt, F., Pedersen, G., & Masson, D. G. (2006). Mechanisms of tsunami generation by submarine landslides: a short review. *Norwegian Journal of Geology/Norsk Geologisk Forening*, 86(3).
- Hilbe, M., & Anselmetti, F. S. (2014). Signatures of slope failures and river-delta collapses in a perialpine lake (Lake Lucerne, Switzerland). *Sedimentology*, 61(7), 1883-1907.
- Huang, X., & García, M. H. (1997). A perturbation solution for Bingham-plastic mudflows. *Journal of hydraulic Engineering*, 123(11), 986-994.
- Imran, J., Parker, G., Locat, J., & Lee, H. (2001). 1D numerical model of muddy subaqueous and subaerial debris flows. *Journal of hydraulic engineering*, 127(11), 959-968.
- Ishimura, D., & Yamada, K. (2019). Paleo-tsunami inundation distances deduced from roundness of gravel particles in tsunami deposits. *Scientific reports*, 9(1), 1-8.
- Jaffe, B., Goto, K., Sugawara, D., Gelfenbaum, G., & La Selle, S. (2016). Uncertainty in tsunami sediment transport modeling. *Journal of Disaster Research*, 11(4), 647-661.
- Kanamori, H. (1972). Mechanism of tsunami earthquakes. *Physics of the earth and planetary interiors*, 6(5), 346-359.
- Kervella, Y., Dutykh, D., & Dias, F. (2007). Comparison between three-dimensional linear and nonlinear tsunami generation models. *Theoretical and computational fluid dynamics*, 21(4), 245-269.
- Kempf, P., Moernaut, J., Van Daele, M., Vandoorne, W., Pino, M., Urrutia, R. and De Batist, M. (2017). Coastal lake sediments reveal 5500 years of tsunami history in south central Chile. *Quaternary Science Reviews*, 161, 99-116.
- Kienle, J., Kowalik, Z., & Murty, T. S. (1987). Tsunamis generated by eruptions from Mount St. Augustine volcano, Alaska. *Science*, 236(4807), 1442-1447.
- Kim, J. (2020a). BingClaw [Software]. Retrieved from <https://github.com/jhkim2/BingClaw>.

- Kim, J. (2020b). BoussClaw [Software]. Retrieved from <https://github.com/jhkim2/BoussClaw>.
- Kim, J., Pedersen, G. K., Løvholt, F., & LeVeque, R. J. (2017). A Boussinesq type extension of the GeoClaw model—a study of wave breaking phenomena applying dispersive long wave models. *Coastal engineering*, 122, 75-86.
- Kim, J., Albertson, J. D., & Taggart, M. W. (2019). Landslide material control on tsunami genesis—the Storegga Slide and tsunami (8,100 years BP). *Journal of Geophysical Research: Oceans*, 124(6), 3607–3627.
- Kremer, K., Anselmetti, F. S., Evers, F. M., Goff, J. and Nigg, V. (2021). Freshwater (paleo) tsunamis—a review. *Earth-science reviews*, 212, 103447.
- Kremer, K., Hilbe, M., Simpson, G., Decrouy, L., Wildi, W., & Girardclos, S. (2015). Reconstructing 4000 years of mass movement and tsunami history in a deep peri-Alpine lake (Lake Geneva, France-Switzerland). *Sedimentology*, 62(5), 1305-1327.
- Kremer, K., Simpson, G., & Girardclos, S. (2012). Giant Lake Geneva tsunami in AD 563. *Nature Geoscience*, 5(11), 756–757.
- Kulikov, E. A., Rabinovich, A. B., Thomson, R. E., & Bornhold, B. D. (1996). The landslide tsunami of November 3, 1994, Skagway Harbor, Alaska. *Journal of Geophysical Research: Oceans*, 101(C3), 6609–6615.
- Lane, E. M., Borrero, J. C., Whittaker, C. N., Mueller, C., Goring, D. G., & Power, W. L. (2017). Probabilistic hazard of tsunamis generated by submarine landslides in the Cook Strait Canyon (New Zealand). *Pure and Applied Geophysics*, 175, 3757–3774.
- LeVeque, R. J. (2002). *Finite volume methods for hyperbolic problems* (Vol. 31). Cambridge university press.
- LeVeque, R. J., George, D. L., & Berger, M. J. (2011). Tsunami modeling with adaptively refined finite volume methods. *Acta Numerica*, 20, 211–289.
- Liapidevskii, V. Y., Dutykh, D., & Gisclon, M. (2018). On the modelling of shallow turbidity flows. *Advances in Water Resources*, 113, 310-327.
- Liapidevskii, V. Y., & Dutykh, D. (2019). On the velocity of turbidity currents over moderate slopes. *Fluid Dynamics Research*, 51(3), 035501.
- Løvholt, F., Bondevik, S., Laberg, J. S., Kim, J., & Boylan, N. (2017). Some giant submarine landslides do not produce large tsunamis. *Geophysical Research Letters*, 44(16), 8463-8472.
- Løvholt, F., Pedersen, G., Harbitz, C. B., Glimsdal, S., & Kim, J. (2015). On the characteristics of landslide tsunamis. *Philosophical Transactions of the Royal Society A: Mathematical, Physical and Engineering Sciences*, 373(2053), 20140376.
- Løvholt, F., Glimsdal, S., & Harbitz, C. B. (2020). On the landslide tsunami uncertainty and hazard. *Landslides*, 17(10), 2301-2315.
- Lynett, P. J., Borrero, J. C., Liu, P. L. F., & Synolakis, C. E. (2003). Field survey and numerical simulations: A review of the 1998 Papua New Guinea tsunami. *Landslide tsunamis: Recent findings and research directions*, 2119-2146.
- Mandli, K. T., Ahmadi, A. J., Berger, M., Calhoun, D., George, D. L., Hadjimichael, Y., Ketcheson, D. I., Lemoine, G. I. and LeVeque, R. J. (2016). Clawpack: building an open-source ecosystem for solving hyperbolic PDEs. *PeerJ Computer Science*, 2, e68.
- Migeon, S., Garibaldi, C., Ratzov, G., Schmidt, S., Collot, J. Y., Zaragosi, S., & Texier, L. (2017). Earthquake-triggered deposits in the subduction trench of the north Ecuador/south Colombia margin and their implication for paleoseismology. *Marine Geology*, 384, 47-62.
- Miller, D. J. (1960). The Alaska earthquake of July 10, 1958: giant wave in Lituya Bay. *Bulletin of the Seismological Society of America*, 50(2), 253-266.
- Monecke, K., Finger, W., Klarer, D., Kongko, W., McAdoo, B. G., Moore, A. L., & Sudrajat, S. U. (2008). A 1,000-year sediment record of tsunami recurrence in northern Sumatra. *Nature*, 455(7217), 1232–1234.

- Moore, J. G., Schweickert, R. A., & Kitts, C. A. (2014). Tsunami-generated sediment wave channels at Lake Tahoe, California-Nevada, USA. *Geosphere*, 10(4), 757-768.
- Mountjoy, J. J., Wang, X., Woelz, S., Fitzsimons, S., Howarth, J. D., Orpin, A. R., & Power, W. (2019). Tsunami hazard from lacustrine mass wasting in Lake Tekapo, New Zealand. Geological Society, London, Special Publications, 477(1), 413-426.
- Nanayama, F., Satake, K., Furukawa, R., Shimokawa, K., Atwater, B. F., Shigeno, K., & Yamaki, S. (2003). Unusually large earthquakes inferred from tsunami deposits along the Kuril trench. *Nature*, 424(6949), 660-663.
- Nigg, V., Wohlwend, S., Hilbe, M., Bellwald, B., Fabbri, S. C., de Souza, G. F., Donau, F., Grischott, R., Strasser, M. and Anselmetti, F. S. (2021). A tsunamigenic delta collapse and its associated tsunami deposits in and around Lake Sils, Switzerland. *Natural Hazards*, 107(2), 1069-1103.
- Okal, E. A. (1988). Seismic parameters controlling far-field tsunami amplitudes: A review. *Natural Hazards*, 1, 67-96.
- Pararas-Carayannis, G. (1992). The tsunami generated from the eruption of the volcano of Santorin in the Bronze Age. *Natural Hazards*, 5, 115-123.
- Paris, R. (2015). Source mechanisms of volcanic tsunamis. *Philosophical Transactions of the Royal Society A: Mathematical, Physical and Engineering Sciences*, 373(2053), 20140380.
- Paris, R., Lavigne, F., Wassmer, P., & Sartohadi, J. (2007). Coastal sedimentation associated with the December 26, 2004 tsunami in Lhok Nga, west Banda Aceh (Sumatra, Indonesia). *Marine Geology*, 238(1-4), 93-106.
- Paris, R., Pelletier, B., Roger, J., Wassmer, P., & Sabatier, P. (2023). Sedimentary evidence of tsunamis in New Caledonia, southwest Pacific. *Marine Geology*, 463, 107116.
- Peterson, C. D., Carver, G. A., Cruikshank, K. M., Abramson, H. F., Garrison-Laney, C. E., & Dengler, L. A. (2011). Evaluation of the use of paleotsunami deposits to reconstruct inundation distance and runup heights associated with prehistoric inundation events, Crescent City, southern Cascadia margin. *Earth Surface Processes and Landforms*, 36(7), 967-980.
- Rabinovich, A. B., Thomson, R. E., & Stephenson, F. E. (1999). The landslide-generated tsunami of November 3, 1994, in Skagway Harbor, Alaska: A case study. *Geophysical Research Letters*, 26(19), 3009–3012.
- Rapuc, W., Arnaud, F., Sabatier, P., Anselmetti, F.S., Piccin, A., Peruzza, L., Bastien, A., Augustin, L., Régnier, E., Gaillardet, J. and Von Grafenstein, U. (2022). Instant sedimentation in a deep Alpine lake (Iseo, Italy) controlled by climate, human and geodynamic forcing. *Sedimentology*, 69(4), 1816-1840.
- Roger, J.H., Bull, S., Watson, S.J., Mueller, C., Hillman, J.I., Wolter, A., Lamarche, G., Power, W., Lane, E., Woelz, S. and Davidson, S., 2024. A review of approaches for submarine landslide-tsunami hazard identification and assessment. *Marine and Petroleum Geology*, p.106729.
- Sammartini, M., Moernaut, J., Anselmetti, F. S., Hilbe, M., Lindhorst, L., Praet, N., & Strasser, M. (2019). An Atlas of mass-transport deposits in lakes. In K. Ogata, A. Festa, & G. A. Pini (Eds.), *Submarine landslides* (pp. 201–226).
- Satake, K. (2012). Satake, K. (2012). Tsunamis generated by submarine landslides. In *Submarine Mass Movements and Their Consequences: 5th International Symposium* (pp. 475-484). Springer Netherlands.
- Strasser, M., & Anselmetti, F. S. (2008). Mass-movement event stratigraphy in Lake Zurich; A record of varying seismic and environmental impacts. In *Beiträge zur Geologie der Schweiz, Geotechnische Serie 95* (pp. 23–41).
- Schäffer, H. A., Madsen, P. A., & Deigaard, R. (1993). A Boussinesq model for waves breaking in shallow water. *Coastal engineering*, 20(3-4), 185-202.
- Schäffer, H. A., & Madsen, P. A. (1995). Further enhancements of Boussinesq-type equations. *Coastal Engineering*, 26(1-2), 1-14.

- Sugawara, D., Goto, K., & Jaffe, B. E. (2014). Numerical models of tsunami sediment transport—current understanding and future directions. *Marine Geology*, 352, 295-320.
- Switzer, A. D., Jones, B. G., Bryant, E. A., & Goff, J. (2012). Bedding structures in Indian tsunami deposits that provide clues to the dynamics of tsunami inundation. Geological Society, London, Special Publications, 361(1), 61–77.
- Synolakis, C. E., Bardet, J. P., Borrero, J. C., Davies, H. L., Okal, E. A., Silver, E. A., Sweet, S., Tappin, D. R. (2002). The slump origin of the 1998 Papua New Guinea tsunami. *Proceedings of the Royal Society of London. Series A: Mathematical, Physical and Engineering Sciences*, 458(2020), 763–789.
- Tappin, D. R., Watts, P., McMurtry, G. M., Lafoy, Y., & Matsumoto, T. (2001). The Sissano, Papua New Guinea tsunami of July 1998—offshore evidence on the source mechanism. *Marine Geology*, 175(1-4), 1-23.
- Thomson, R. E., Rabinovich, A. B., Kulikov, E. A., Fine, I. V., & Bornhold, B. D. (2001). On numerical simulation of the landslide-generated tsunami of November 3, 1994 in Skagway Harbor, Alaska. *Tsunami research at the end of a critical decade*, 243-282.
- Toro, E. F. (2001). *Shock-capturing methods for free-surface shallow flows*. Wiley.
- Urgeles, R., & Camerlenghi, A. (2013). Submarine landslides of the Mediterranean Sea: Trigger mechanisms, dynamics, and frequency-magnitude distribution. *Journal of Geophysical Research: Earth Surface*, 118(4), 2600–2618.
- Van Rensbergen, P., De Batist, M., Beck, C., & Chapron, E. (1998). High-resolution seismic stratigraphy of late Quaternary fill of Lake Annecy (northwestern Alps): evolution from glacial to interglacial sedimentary processes. *Sedimentary Geology*, 117(1-2), 71–96.
- Waldmann, N., Vasskog, K., Simpson, G., Chapron, E., Støren, E.W.N., Hansen, L., Loizeau, J.L., Nesje, A. and Ariztegui, D. (2021). Anatomy of a catastrophe: Reconstructing the 1936 rock fall and tsunami event in Lake Lovatnet, western Norway. *Frontiers in Earth Science*, 9, 671378.
- Ward, S. N. (1980). Relationships of tsunami generation and an earthquake source. *Journal of Physics of the Earth*, 28(5), 441-474.
- Ward, S. N. (2001). Landslide tsunami. *Journal of Geophysical Research: Solid Earth*, 106(B6), 11201-11215.
- Watts, P. (1998). Wavemaker curves for tsunamis generated by underwater landslides. *Journal of waterway, port, coastal, and ocean engineering*, 124(3), 127-137.
- Watts, P. (2000). Tsunami features of solid block underwater landslides. *Journal of Waterway, Port, Coastal, and Ocean Engineering*, 126(3), 144-152
- Wilhelm, B., Arnaud, F., Sabatier, P., Magand, O., Chapron, E., Courp, T., Tachikawa, K., Fanget, B., Malet, E., Pignol, C. and Bard, E. (2013). Paleoflood activity and climate change over the last 1400 years recorded by lake sediments in the north-west European Alps. *Journal of Quaternary Science*, 28(2), 189-199.
- Yamada, Y., Kawamura, K., Ikehara, K., Ogawa, Y., Urgeles, R., Mosher, D., Chaytor J., Strasser, M. (2012). Submarine mass movements and their consequences. In *Submarine mass movements and their consequences, advances in natural and technological hazards research*, 31st edn. Springer, Dordrecht, 1–12
- Zengaffinen, T., Løvholt, F., Pedersen, G. K., & Muhari, A. (2020). Modeling 2018 Anak Krakatoa Flank Collapse and Tsunami: effect of landslide failure mechanism and dynamics on tsunami generation. *Pure and Applied Geophysics*, 177, 2493-2516.